Local Reconstruction for Three Dimensional Terahertz Imaging Using a CW Quantum Cascade Laser

X.X. Yin and B.W.-H. Ng and D. Abbott
School of Electrical & Electronic Engineering, The University of Adelaide, Australia
e-mail: dabbott@eleceng.adelaide.edu.au

J. A. Zeitler and K. L. Nguyen and L. Gladden
Department of Chemical Engineering, University of Cambridge, CB2 3RA, UK

Abstract ***This paper reports on the local reconstruction of a region-of-interest from 3D terahertz imaging data obtained via a quantum cascade laser (QCL). It is an important step in understanding the trade-off between wavelet based techniques and traditional filtered back projection (FBP) for local reconstruction of terahertz images. The advantage of local reconstruction is a reduction in measurement time. Segmentation algorithms are applied to the reconstructed images with low contrast for analysis of optical properties of target objects with complex contours.***

Keywords: computed tomography, discrete wavelet transforms (DWT), filtered back projection, Terahertz, quantum cascade laser

1 Introduction

Terahertz radiation (T-ray) spans the frequency range from 0.1 THz to 10 THz in the electromagnetic spectrum [1]. The potential based on high power Quantum Cascase Lasers (QCLs) is of interest with advantages for biomedical imaging and security detection [2]. In contrast with traditional THz pulsed imaging, QCLs provide high power sources of continuous wave (CW) radiation to achieve deeper penetration of samples, which has been identified as one of four principal challenges for terahertz tomography [3]. The CW terahertz imaging methods use THz of constant intensity and further offer improved signal-to-noise performance, but with the difficulty of resolving the material absorption from scattering [4]. This paper investigates the scattering of terahertz CW radiation with QCLs and applies local reconstruction algorithms to a sample target with complex contours.

Unlike Magnetic Resonant Imaging (MRI) and X-ray imaging, which realise parallel scanning using multiple point detection, point to point detection is the fundamental scheme of terahertz scanning. However, T-rays are non-ionising unlike X-rays and allow imaging of relatively small objects compared to MRI. To overcome the point-to-point scanning disadvantage, it is important to reduce the time of terahertz measurements. The main goal of this paper is to present a wavelet based reconstruction algorithm for QCL-based terahertz computed tomography and to show how this algorithm can be used to rapidly reconstruct the region of interest (ROI) with a reduction in the number of required measurements. We illustrate filtered sinograms and reconstructed images in the region of interests at different measurement heights, using as sample a polystyrene clown's head with a hollow inside. It is found that local reconstructions of the target's internal structure take on a number of different shapes since the various contours of the target physically change the estimated optical properties of the object. Local computed tomography (LCT) achieved from scaling functions shows better resultant reconstruction with improved smoothness and reduced artifacts.

1.1 Introduction to T-ray QCL

QCLs are semiconductor injection lasers, based on quantum semiconductor structures that are grown by molecular beam epitaxy and designed by band structure engineering [2]. Quantum cascade lasers, in principle, are realised via intersubband transitions in a multiple-quantum-well (MQW) heterostructure [6]. Different from the conventional diode laser techniques, QCLs only involve a transition of the electron that occurs between the conduction bands (intersubband) instead of transitions from conduction

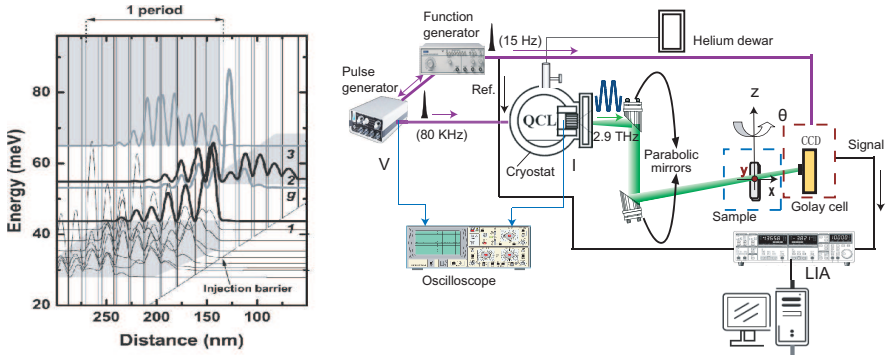

(a) (b)

Figure 1: *(a) One period of the conduction band profile regarding a bound-to-continuum design of the semiconductor layer sequence. The upper, and lower states of the laser transition and the injector miniband ground state are labelled 2, 1, and g, respectively. The transition energy, given by the energy difference between 2 and 1, is 12 meV. At alignment the wave functions of the upper and lower state are broadly overlapping. The upper state wave function is concentrated mainly in the two quantum wells adjacent to the injection barrier, reducing the overlap with the lower energy states in the injector miniband, thereby enhancing the non-radiative upper state lifetime. Electrons are injected into the upper state from state g through injection barrier. The active region consists of 85 identical repeat periods. After [5]. (b) Experimental apparatus for a THz QCL imaging system used to realise THz CT. The sample is placed on a rotational stage for multi view angles, which is mounted on a xyz linear stage to perform 3D scanning.*

into valence bands. As a result, the emission wavelength can be controlled by the thickness of the MQW, and the intrinsic high-power capabilities of the lasers make possible the cascading process, in which each electron generates several tens of photons in superlattice structures. In addition, intersubband transitions are characterized through ultrafast carrier dynamics and band-structure engineering is available to successfully control the electron flow and thus increase population inversion, which ultimately controls the laser threshold [6]. Fig. 1(b) shows a schematic diagram of a THz bound-to-continuum (BTC) QCL design, for the current THz experiment.

The current THz QCL is a GaAs-AlGaAs bound-to-continuum superlattice design, emitting at 2.9 THz (103 μm), and grown by molecular beam epitaxy [7]. This device typically operates up to 95 K in pulse mode and delivering 70 mW per facet peak power. Illustrated in Fig. 1(a), the QCL is mounted on the cold finger of a continuous-flow helium-cooled cryostat maintaining a heat-sink temperature of 4.2 K. The emission is collected and focused with a pair of off-axis parabolic mirrors onto the sample. The sample is mounted on a rotational stage, which is itself mounted on an $x-y-z$ translational stage. This current terahertz imaging setup achieves point to point detection. The linearly moving stage enables parallel scanning along the x-axis with linear velocity of 20 mm/s and a rotating stage, labelled by θ, allows projections of an object to be taken at a number of projection angles with a rotary velocity of 4 degree/s. The y-axis is perpendicular to the paper. The z axis motion allows the sample to move vertically in order to obtain cross section images at various heights. The transmitted beams are detected by a Golay cell. The power incident on the sample, including the effects of the transmission of the cryostat window, is typically ∼35 mW (peak). The signal-to-noise ratio in the absence of a sample in the beam is 20 dB. For more detail refer to [8].

2 Methodology

2.1 An Overview of CT

The filtered back projection algorithm (FBP) is often used in the calculation of the inverse Radon transform [9]. Normally, this algorithm begins with a collection of *sinograms* obtained from projection measurements. A sinogram collects points in a projection space. It is simply a collection of the projections at all the projection angles. A 1D projection at each projection angle is a linear integral of the image intensity along the projection offset.

2.2 2D Wavelet Based CT

Wavelet transforms play an important role in many image processing tasks. They have the advantage of much improved joint time-frequency localisation over Fourier transforms. In practice, it is nearly always implemented using digital filters and downsamplers. In two dimensions, the discrete version of a wavelet transform can be realised by a 2D scaling function, and three 2D wavelets, which are calculated by taking the 1D wavelet transform separately along the rows and columns of an image [10].

In order to achieve 2D wavelet reconstruction, the wavelet coefficients of a function on $\mathbf{R}^2$ space are computed directly on the Radon transform data. This method enables reduced computation compared to the wavelet coefficients obtained, after conducting wavelet transforms in a reconstructed image. Additionally, the wavelet coefficients are calculated locally allowing the local reconstruction to yield local computed tomography [11]. The main formulas for 2D DWTs, on projection data, for the reconstruction of a CT image are introduced, which are realised via performing separate wavelet transforms on 1D projection data. The function enables image reconstruction as the conventional inversion of the Radon transform method, while the ramp filter is replaced by the wavelet ramp filter.

A significant characteristic of wavelet functions is that they must have a number of vanishing moments. Hilbert transforms of functions with many vanishing moments have been shown to decay very rapidly at infinity. In other words, a wavelet function with compact support allows a local basis to maintain its localised features after Hilbert transformation [11]. Therefore, the wavelet and scaling coefficients for a wavelet basis can be calculated after applying the projections passing through the region of interest plus a margin for the support of the wavelet and scaling ramp filters. These reconstructed coefficients, in this experiment, are then directly applied to the inverse wavelet transforms for terahertz image reconstruction [11]. For the current image reconstruction, only one 2D wavelet transform level is used for simplicity.

3 Implementation

3.1 Practical Consideration

In this paper, one set of terahertz QCL data is considered for LCT: the nested structure of a polystyrene clown's head with hole inside, see Fig. 2(a). The target sample is imaged in 12 slices, from bottom to top at twelve different heights, 5 mm apart. The diameter of the hole is 10.1 ± 0.2 mm measured directly from the target. For the current local reconstruction, only the second to fifth image slices are considered with the hole going through at the tilted angle of 43°. The center of the hole at the first slice is also centered at the bottom cross-section. The target layers, labelled from Slice 1 to Slice 4, with 289 projections at each of 18 projection angles covering a 180° projection area in a 250×250 image, in addition to the fifth slice, which includes 268 projections at each projection angle.

In this work, we experiment with the separate 2D wavelet technique and traditional filtered back projection algorithm using terahertz tomographic data by modifying the measured projections. In local reconstruction, artifacts are commonly found close to the boundary of the region of exposure (ROE), which can readily be observed in the application to terahertz CT data. This modification involves an extrapolation technique to avoid edge effects due to sinogram truncations. It is also observed that approximate coefficients of a scaling function show good localised features in the local reconstruction using our algorithm, where the reconstructed image shows a smooth and uniform segmentation effect compared to local reconstruction using FBP.

3.2 Error Analysis

In order to test the performance of the local imaging system, we compare binary grey-level images obtained via segmentation after back projection reconstruction. The cases considered include: a truncated version of global CT via FBP, the proposed LCT via wavelet transforms, and LCT via FBP, all carried out over the region of interest. The difference is calculated between the ground truth (determined analytically) and each of the resultant segments at four different measurement heights. The error rate is regarded as the number of mis-labelled pixels divided by the total number of pixels of the binary grey-level image from the target sample. For further validation of the segmentation results, slopes computed from the centroids of the segments at two different heights are compared with the known slope of the linear hole structure inside the target, which leads to another error—error in slope.

3.2.1 Characteristics of a hole image

The typical local reconstruction reveals a single hole through the sample. There are several notable characteristics of this local image, see Fig. 2(b), which

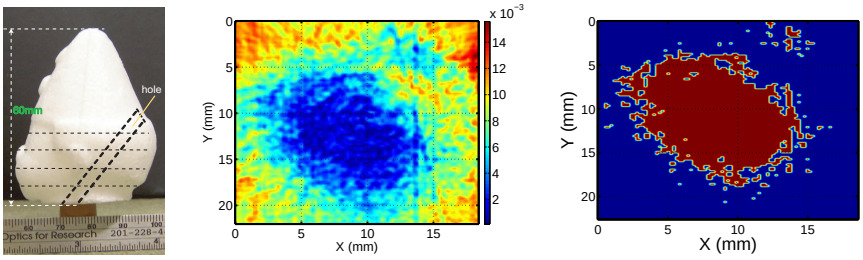

(a) (b) (c)

Figure 2: *(a) A photograph of the side face of the clown's head. (b) A typical local reconstruction, containing a single hole. (c) The result of applying Otsu's thresholding method on (b).*

are common to typical local reconstructions of the hole embedded in a 3D target at the difference slices by different image reconstruction algorithms. Firstly, the contrast of intensities between the hole and background is low, and is so difficult to distinguish. However, the average intensity of the background is often roughly uniform across all reconstructions, with a sightly darker region within the hole position than the background. The hole embedded in the target physically changes the optical properties of the target, depending on the slice shape and hole distance from the detector at each different measurement height. These various contours of the different slices result in varying degrees of optical distortion due to light scattering. As a further source of complication, a longer path length from the hole center position at each slice to the laser results in larger absorption. The 3D local reconstruction of the hole target, takes on a number of different shapes in the different slices. As a result, the boundary of the hole can be rather difficult to define. Due to variations in intensity, both within the hole position and in the background, portions of the hole appear to blend gradually into the background, without creating a distinct boundary.

3.2.2 Segmentation strategy

A popular segmentation scheme is image thresholding [10], which can be regarded as a form of pixel classification. Grey-level intensity as a feature value is associated with each pixel of an image. The calculated threshold is compared with the feature value to map the pixel onto one of two groups, objects and background regions. The threshold method applied in the paper is proposed by [12]. It is based on a statistical analysis of variance. It has been suggested that this approach is preferred among many popular global threshold methods, especially since it performs well in situations where there is little contrast between background and object [13].

The segment is calculated by a single threshold level for the entire image. This is a reasonable suggestion, since (i) we are not concerned with finding the boundary of the object cross section, so we effectively only have a two-class problem, and (ii) thresholding just for the hole is followed by post-processing to clean up the segmented region. We considered multi-threshold approaches but eventually chose a single threshold strategy for simplicity, as we found that sufficient for the aims of this experiment.

Thresholding the image can incur two kinds of noise: background pixels misclassified to the hole sample, which produce small disjoint hole components in addition to the hole region, and hole pixels misclassified as the background, which produce gaps in the hole region of interest, see Fig. 2(c). Misclassification of either target sample of interest or background pixels near the hole boundary can also produce an extremely coarse boundary. In order to obtain the boundary representation of the hole region, region-based segmentation operations and morphological operations [10] are combined to repair the gaps in the hole region of interest and improve the smoothing boundaries. This approach aims to apply *region growing* on a typical local reconstruction, which is represented as follows. Eight neighbor pixels are used as *seed pixels*. There are four starting points from four sets of seed pixels, which are applied for segmentation. Those starting points are positioned at the central point of the ROI or around the image center. The four sets of seed pixels move from pixel to pixel along four quadrants of the coordinates, separately, starting from the four starting points. Predefined criteria are selected depending

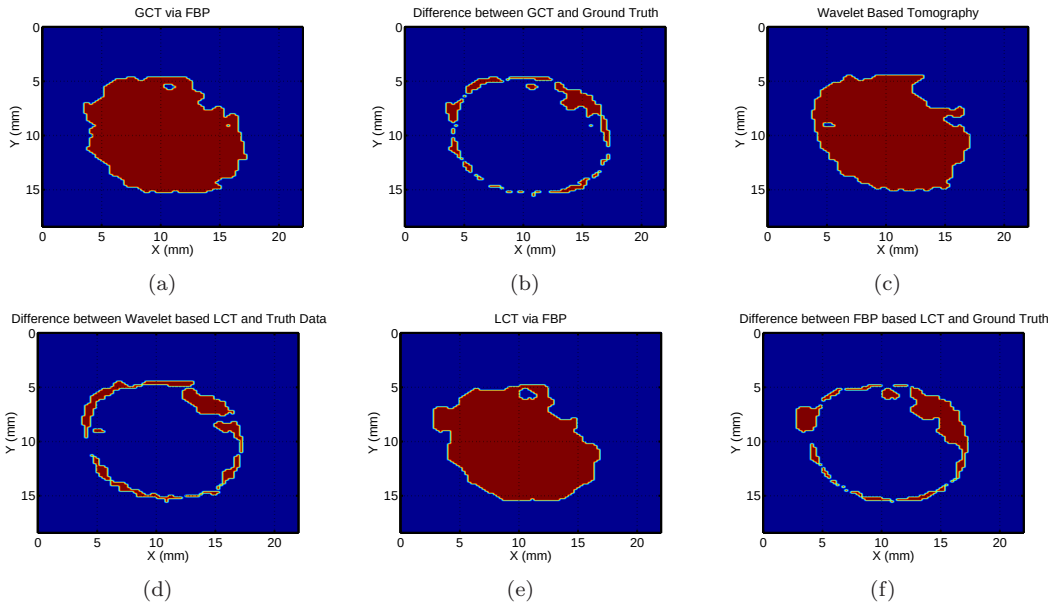

Figure 3: *Illustration of the resultant segments and the difference at Slice 1. (a) The segment in the ROI using traditional FBP and global data. (b) The difference between the segment of (a) and the simulation. (c) The segment in the ROI using scaling function and local data. (d) The difference between the segment of (c) and the simulation. (e) The segment in the ROI using traditional FBP and local data. (f) The difference between the segment of (e) and the simulation.*

on the broken characters that are shown in each reconstruction. The maximum length of the breaks in the eight neighboring pixels is known to be two to four pixels. During the processing, we assign 1 to the pixel satisfying the selection criteria, otherwise we set the pixel to zero. This region growing is conducted repeatedly till a single, connected hole region of interest appears without gaps.

In some cases, artifacts can be mistaken for the hole region of interest. Therefore a simple mechanism is designed to reject artifacts during the segmentation procedure. After region growing is used to regions obtained by thresholding the local reconstruction, a simple criterion is adopted to examine the length feature of the segmented hole region of interest, to ensure that the correct hole target region is selected. In this way, large artifacts can be eliminated, and small artifacts can be removed by region growing.

For calculation of the error of segmentation based reconstruction, we compare each of the resultant segments with the ground truth. The error rate is regarded as the difference between the resultant segment and truth data, with the total number of pixels then divided by the number of pixels of the segment from ground truth. The ground truth is known to be an ellipse with semimajor axis of 13.2 ± 0.6 mm and semiminor axis of 10 ± 0.8 mm along with the rotation angle of $8 \pm 2°$.

4 Reconstruction Results

Four situations are analyzed for this target sample. The sizes of ROE and ROI at each slice heights are the same, respectively, exclude the Slice 2. They are: (i) the first slice (Slice 1) from the four slices with an Region of Exposure (ROE) of diameter 189 pixels and an ROI of diameter 110 at the center of the image; (ii) the second slice (Slice 2) with an ROE of diameter 230 pixels and an ROI of diameter 195 at offcenter, for ramp filter application to the image, while an ROI of diameter 160 at offcenter applied to the wavelet based reconstruction; (iii) the third slice (Slice 3) with an ROE of diameter 209 pixels and an ROI of diameter 150 at an offcenter; (iv) the fourth slice (Slice 1) with an ROE of diameter 196 pixels and an ROI of diameter 140 at offcenter. Each of dataset has a pixel interval of 0.5 mm.

4.1 Slice One

The sinogram at Slice 1 with zero padding for nonlocal data. The reconstructed images at an off-center area with a radius of 95 pixels using the current local reconstruction algorithms. A 250×250 pixel image of the clown's head target is recovered from scaling coefficients using local data, and the BioSpline 2.2 biorthogonal basis is used. The same wavelet basis is applied to all the slices for wavelet based reconstructions. Two dimensional inverse wavelet transforms are conducted on the four reconstructed subimages to obtain the image with full package of wavelet based image reconstruction. For simplicity, however, the current algorithm only utilises the approximate image reconstruction.

The segment of the reconstructed image via scaling function Fig. 3(c), shows smoother contours with reduced artifacts than the segmented image via the FBP algorithm, Fig. 3(e). In addition, the scaling function leads to an LCT with small difference in segment from the ground truth, Fig. 3(d), compared to the difference in segment, Fig. 3(f), between the traditional local CT and the truth data, though a slightly large difference in segmentation from the truth data compared with the difference, Fig. 3(b), between traditional reconstructed segment in ROI using global data, Fig. 3(a), and the ground truth. The relative error rates using different algorithms are shown in Table 3. For this slice, the segments show high quality reconstruction, whether from the traditional FBP algorithms using global and local data or from LCT with the scaling function, owing to the uniformity in the target sample and the relatively short path length to the hole position. More segments achieved from slices 2 to 4 are omitted due to page limitations.

4.2 Segment Evaluation

In order to evaluate the current segmentation, in this experiment, we exploit the fact that the internal structure, the hole, is straight. This implies that the segmented hole positions should be proportionally displaced from each other, since they correspond to constant increments of 5 mm in height. To obtain this measurement, we find the centroid of the extracted hole for each height, L1-L5, and the resultant x and y locations recorded in Table 2, and the slopes between each of the two centroids from any of two slices recorded in Table 3 illustrates the error rate for the three reconstructed algorithms: traditional global reconstruction, scaling function used for LCT and traditional local reconstruction via FBP. For similarity, in the following tables, GCT denotes global CT via FBP algorithms, ALCT denotes the approximate reconstruction of local CT WTs, and FLCT denotes the local CT via FBP algorithms.

Table 1: The size of both the ROE and the ROI at four target heights and via the three different reconstructed algorithms, in units of mm.

algorithms	radius	L1	L2	L3	L4
approximate LCT	ROE	95	115	105	99
	ROI	55	80	75	70
LCT via FBP	ROE	95	115	105	99
	ROI	55	99	75	70

Table 1 records the radii of the ROE and ROI at different heights via applying scaling function and FBP algorithms for reconstruction. It is found that, at the height L1, the radii of the ROE and ROI are the smallest among all the local reconstructions at the measured heights from L1 to L4, owing to the smaller optical distortion, but with the bigger value of (ROE-ROI) than the local reconstructions for the other target heights. At the height L2, biggest radii of ROE and ROI are applied to LCT, though, the scaling function for the reconstruction needs smaller radius of ROI than FBP based reconstruction. In other words, it is possible for wavelets to acquire the LCT using smaller exposure area, which shows the superior ability of wavelet to achieve local reconstruction. With the reduced optical distortion and improved reconstruction accuracy at the heights of L3 and L4, there are reduced radii of the ROE and ROI to be employed for the local reconstruction of the similar size of hole cross-section. The smaller scattering needs smaller size of radii of ROE and ROI to recover the local image, vice versa.

Table 2 is the centroid coordinates of the extracted hole cross-section for each height, which are used for the calculation of slopes at different target heights.

Table 2: The centroid coordinates of the extracted hole for each height, with units of mm.

algorithms	coordinates	L1	L2	L3	L4
GCT via FBP	x	134	157	185	207
	y	118	124	130	136
ALCT	x	135	156	184	198
	y	116	126	132	138
FLCT	x	136	154	191	202
	y	121	130	134	141

The slopes calculated via using global data and FBP algorithms show similar slopes, which mean a linear structure can be reconstructed via applying global data and FBP algorithms. It also validates the current segment detection. The average slope is 0.2450 with an

error of 0.6875 compared to the ground truth. As strong scattering caused by the variable shape of the target object at different slices, the slope angle of the hole appears smaller than expected.

The slopes via the scaling function for local reconstructions can recover the linear structure with an average slope of 0.3355, with reduced average error of 0.5970. The larger variations in slope compared with the GCT shows that the wavelet reconstruction is sensitive to the physical changing of optical properties of the imaging.

The slopes via FBP algorithms for local reconstructions can recover the linear structure with average slope of 0.3467 and the average error of the linear reconstruction is 0.5858. The local reconstruction via FBP recovers a linear structure of the hole structure in its 3D position with inferior performance compared to the remaining two reconstruction algorithms.

Table 3: The error rate from each of the four heights and each of the three reconstructed methods.

algorithms	L1	L2	L3	L4
GCT	0.1380	0.7112	0.3042	-0.3761
ALCT	0.1824	0.5306	0.2664	-0.3532
FLCT	0.2136	0.5350	0.2224	-0.3552

Table 3 records the calculated error rate. The reconstructions are achieved by using a FBP algorithm and global data; approximate local reconstruction; and local reconstruction using a FBP algorithm. It shows that the reconstructed error is the smallest at L1 and the largest at L2, due to the increased scattering caused by the variations in the target sample's shape at the height L2 compared with L1. The error at L3 is reduced compared to L2 since absorption counteracts the effect of the scattering. The error at L4 is negative, since the effect of optical absorption dominates optical scattering.

5 Conclusion

We have presented a wavelet based algorithm for tomographic reconstruction of a target from its Radon transform of terahertz signals measured using a QCL. Based on the observation that for some wavelet bases, with sufficient zero moments, the scaling and wavelet functions have essentially the same support after ramp filtering, we were able to show that this algorithm can achieve better performance in locally reconstructing the internal structure of a 3D target. Segmentation is employed for the analysis of the quality of the reconstruction, and it was found that performance was dependent on the distortion arising from the shape of the different target cross-sections in a 3D space. A scaling function for the reconstruction shows a slight structure distortion in the reconstruction of a 3D structure compared to GCT, due to the use of local data. A potential direction for future work is the investigation of using multi-class segmentation techniques [14] on the reconstructed images.

References

[1] D. Abbott and X.-C. Zhang, "T-ray imaging, sensing, and retection," *Proceedings of the IEEE*, vol. 95, no. 8, pp. 1509–1513, 2007.

[2] S. M. Kim, F. Hatami, J. S. Harris, A. W. Kurian, J. Ford, D. King, G. Scalari, M. Giovannini, N. Hoyler, J. Faist, and G. Harris, "Biomedical terahertz imaging with a quantum cascade laser," *Applied Physics Letters*, vol. 88, pp. Art. No. 153903, 2004.

[3] X. C. Zhang, "Three-dimensional terahertz wave imaging," *Philosophical Transactions Royal Society London A*, vol. 362, pp. 283–299, 2004.

[4] V. Ntziachristos, J. Ripoll, L. V. Wang, and R. Weissleder, "Looking and listening to light: the evolution of whole-body photonic imaging," *Nature Biotechnology*, vol. 23, no. 3, pp. 313–320, 2005.

[5] J. Alton, *Bound-to-Continuum THz Quantum Cascade Lasers (PhD Thesis)*, The University of Cambridge, Cambridge, U.K., 2005.

[6] C. Gmachl, F. Capasso, D. L. Sivco, and A. Y. Cho, "Recent progress in quantum cascade lasers and applications," *Report on Progress in Physics*, vol. 64, pp. 1533–1601, 2001.

[7] S. Barbieri, J. Alton, H. E. Beere, J. Fowler, J. Ford, E. H. Linfield, and D. A. Ritchie, "2.9 THz quantum cascade lasers operating up to 70 K in continuous wave," *Applied Physics Letters*, vol. 85, no. 10, pp. 1674–1676, 2004.

[8] K. L. Nguyen, L. J. Michael, L. Gladden, C. H. Worrall, P. Alexander, H. E. Beere, M. Pepper, D. A. Ritchie, J. Alton, S. Barbieri, and E. H. Linfield, "Three-dimensional imaging with a terahertz quantum cascade laser," *Optics Express*, vol. 14, no. 6, pp. 2123–2129, 2006.

[9] A. C. Kak and M. Slaney, *Principles of Computerized Tomographic Imaging*, IEEE Press, New York, 1988.

[10] R. C. Gonzalez and R. E. Woods, *Digital Image Processing*, Prentice-Hall, Inc., New Jersey, 2002.

[11] F. Rashid-Farrokhi, K.J.R. Liu, C.A. Berenstein, and D. Walnut, "Wavelet-based multiresolution local tomography," *IEEE Transactions on Image Processing*, vol. 6, no. 10, pp. 1412–1430, 1997.

[12] N. Otsu, "A threshold selection method from gray-level histograms," *IEEE Transactions on Systems, Man, and Cybernetics*, vol. SMC-9, pp. 62–66, 1979.

[13] K. Wu, D. Gauthier, and M. D. Levine, "Live cell image segmentation," *IEEE Transactions on Biomedical Engineering*, vol. 42, no. 1, pp. 1–12, 1995.

[14] P.S. Liao, T.S. Chew, and P.C. Chung, "A fast algorithm for multilevel thresholding," *Journal of Information Science and Engineering*, vol. 17, pp. 713–727, 2001.